Materials Characterization 169 (2020) 110576

Contents lists available at ScienceDirect

Materials Characterization

journal homepage: www.elsevier.com/locate/matchar

The role of microstructure and local crystallographic orientation near porosity defects on the high cycle fatigue life of an additive manufactured Ti-6Al-4V

Muhammad Shamir, Abdul Khadar Syed*, Vit Janik, Romali Biswal[1], Xiang Zhang

Institute for Future Transport and Cities, Faculty of Engineering, Environment and Computing, Coventry University, Coventry CV1 5FB, UK

ARTICLE INFO

Keywords:
Additive manufacturing
Crack initiation
Porosity
Schmid factor
Titanium alloy

ABSTRACT

Titanium alloys such as Ti-6Al-4V built by most of the additive manufacturing processes are known to contain process induced defects, non-conventional microstructure and strong crystallographic texture; all of which can affect the fatigue strength. In this study we evaluated the effect of crystallographic orientation of α and α lath width around gas pore defects on the high cycle fatigue life of Wire + Arc Additive Manufactured Ti-6Al-4V by means of Electron Back Scattered Diffraction. Here we show that variations in crystallographic orientation of α lath and its width in the vicinity of the crack initiating defect were the main reasons for the considerable scatter in fatigue life. Pyramidal slip systems with high Schmid factor active around the defects resulted in longer fatigue life compared to pyramidal slip with lower Schmid factor. In the absence of pyramidal slip, cracks initiated from active prismatic slip systems. When considering the influence of the microstructure, a higher number of smaller α laths around the defect resulted in longer fatigue life, and vice versa. Overall, the fatigue crack initiation stage was controlled collectively by the complex interaction of porosity characteristics, α lath width and its crystallographic orientation at the crack initiation location.

1. Introduction

Fatigue performance of titanium alloy Ti-6Al-4V (Ti64) produced by additive manufacturing (AM) processes suffers from defects, process-dependent microstructures and strong crystallographic texture of grains [1]. Since Ti64 is a commonly used high strength alloy, considerable research has been carried out on its fatigue performance when built by various AM processes in both as-built and post processed conditions [2–4]. Presence of defects in the as-built AM Ti64 causes stress concentration, and as a result, early crack initiation may occur, resulting in poor fatigue performance [3,5]. However, post-deposition heat treatment such as hot isostatic pressing (HIPing) can be applied to reduce the defect size and its density [6]. Nevertheless, some defects were found to be still present even after HIPing [7]. It has been shown previously that defects with sizes as small as 20 μm caused stress concertation and led to crack initiation and fatigue failure [3].

When considering the location of the defect within the deposited material, surface or subsurface defects are more detrimental than embedded defects [6,8]. Leuders et al. [9] attributed the fatigue failure of selective laser melted Ti64 to the initiation of fatigue cracks from the defects that were not only close to the sample surface but also in the interior of the specimens, even in the HIPed condition. Leuders et al. [9] also demonstrated that it was not the largest defect that led to the fatigue failure but the most clustered ones, owing to multiple defect interactions [9,10]. A comparison of the fatigue strength sensitivity to defects for AM Ti64 was presented in [11], which concluded that the defect characteristics (size, shape and location) affected the fatigue strength. Biswal et al. [13] investigated the effect of defect size, shape and location on the stress concertation factor by finite element analysis and found that the stress concentration factor was sensitive to the defect shape and location, but insensitive to the defect size [12,13]. If the distance of a defect to the nearest free surface was less than four times of its diameter, the defect was considered to be a subsurface defect, with stress concentration factor increasing as defect moving closer to the free surface [13]. Murakami used a fracture mechanics approach to analyse the stress intensity factor and its variation as a function of the ratio of defect radius to the distance from the defect centre to the surface. He found that if the ratio is less than 0.8, then the stress

* Corresponding author.
E-mail addresses: shamirm@uni.coventry.ac.uk (M. Shamir), abdul.syed@coventry.ac.uk (A.K. Syed), vit.janik@coventry.ac.uk (V. Janik), r.biswal@cranfield.ac.uk (R. Biswal), xiang.zhang@coventry.ac.uk (X. Zhang).
[1] R Biswal current address is: Welding Engineering and Laser Processing Centre, Cranfield University, Cranfield MK43 0AL, UK.

https://doi.org/10.1016/j.matchar.2020.110576
Received 5 February 2020; Received in revised form 6 August 2020; Accepted 14 August 2020
Available online 21 August 2020

intensity factor is equal to that of an isolated defect and there is no interaction between the defect and the free surface. However, the stress intensity factor is dependent on the size of the defect [14].

Fatigue strength sensitivity to defects for various AM built Ti64 as presented in [11] also showed that the microstructure surrounding the defect also influenced the fatigue life. It is worth noting that the microstructures produced by AM processes are complex and often vary spatially within a build [1]. In conventionally produced Ti64, three distinct microstructures are normally obtained depending on the selected thermo-mechanical processing route, i.e. fully lamellar, fully equiaxed, and bi-modal (duplex) microstructures containing equiaxed primary α (α_p) in a lamellar α + β matrix [15]. Depending on the cooling rate, the fully lamellar microstructure can further transform into either Widmanstätten (basketweave) or martensitic microstructure. The detailed description of processing routes to achieve these microstructures can be found in [15].

In HCP materials such as titanium alloys, the phase transformation from β (bcc) to α (hcp) takes place via a specific Burgers orientation relationship {110}β || (0001)α and the ⟨111⟩β || ⟨1120⟩α. A single β grain can transform to a total of 12 different α orientation variants during the transformation, leading to a crystallographic texture that is cooling rate dependent [16]. When materials are subjected to cyclic loading the damage accumulation is strongly localised and is directly linked to a specific plastic deformation mechanism (i.e. slip and twinning). Bridier et al. [17] investigated the fatigue crack formation mechanisms in a forged Ti64 and showed that fatigue cracks always initiated within primary α grains with both prismatic and basal slip planes characterised by high Schmid factor. However, easier prismatic slip activation was observed compared to basal due to the lower strength of prismatic slip systems. They have also concluded that combination of high Schmid factor and high tensile stress is required for crack formation on basal planes, whereas crack initiation on prismatic planes involves surface roughening mechanism due to high Schmid factor and single slip. In the case of lamellar colonies, the cracks initiated from prismatic slip planes parallel to the lamellar direction [18,19]. When considered the AM built Ti64, Åkerfeldt [20] investigated fatigue crack growth in laser metal deposited Ti64. Fatigue crack paths analysed using electron back scattered diffraction (EBSD) confirmed that the cracks mostly preferred to grow along the pyramidal slip system. However, crack also propagated through the basal and prismatic slip systems in fewer areas [20]. Åkerfeldt [20] concluded that the presence of large α colonies with same crystallographic orientation caused tortuosity within the crack propagation areas. This might have contributed to the lower crack growth rates as crack continuously deflected during its propagation. Furthermore, large areas of local crystallographic misorientation were observed in regions around defects indicating inhomogeneous stress distribution [20]. From this it is evident that the presence of strong crystallographic orientation within the material and at and around the defects influence the fatigue life of AM built materials.

Wire + Arc Additive Manufacturing (WAAM) is able to produce fully dense Ti64 parts and is therefore advantageous compared to other AM processes. When comparing the tensile properties, WAAM Ti64 showed 8% and 13% higher yield strength (YS) and tensile strength (TS) compared to cast Ti64, and 10% and 7% lower YS and UTS compared to wrought Ti64. If considering the fatigue properties of WAAM Ti64, relatively few studies were performed to understand the effect of heterogenous microstructure and microstructural defects. High cycle fatigue properties of WAAM Ti64 deposited using single bead deposition strategy showed a 10% higher fatigue life compared to the mill annealed Ti64 [21]. Although the WAAM process is able to deliver high density parts [21,22], feedstock contamination may occur during the deposition process that can result in gas pore defects and lead to crack initiation from these defects [21,22]. Additionally, a large scatter of fatigue life values was reported both in WAAM Ti64 [21,22] and also in other AM processed Ti64 [3] which is the direct consequence of the

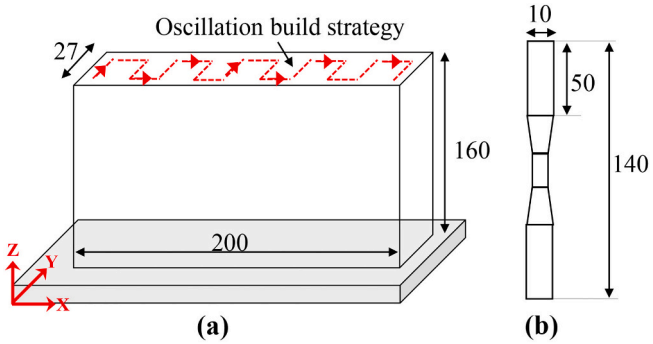

Fig. 1. Schematic illustration of (a) WAAM Ti64 wall, (b) geometry and dimensions of a fatigue sample (unit: mm, not to scale). Build direction was along the *Z*-axis and torch movement was oscillated along the *Y*-axis for each layer.

defects presence in the as-built material. Life prediction models based solely on the continuum mechanics could not explain the scatter found in the results presented in [13,22], because the fatigue properties are controlled by defects as well as the microstructure [21–26]. Therefore, a comprehensive understanding of defects-microstructure-crystallographic orientation relationship under cyclic loading is necessary. Hence, the present study is focused on investigating the reasons of scatter in fatigue life presented in [22] with the aim to identify the competing factors from defects, the microstructure and crystallographic orientation of α in an as-built WAAM Ti64 material.

2. Materials and experimental methods

The experimental material was produced by previously optimised WAAM process [22] using a 1.2 mm diameter grade 5 Ti64 wire. An oscillation build strategy in which both wire feeder and plasma torch oscillate were employed to build a 27 mm thick WAAM Ti64 wall. Schematic of the oscillation build strategy is presented in Fig. 1a. Further detailed description of the build process, deposition parameters and chemical composition of Ti64 wire can be found in [22]. X-ray computed tomography (X-ray CT) was used to measure the density and average porosity size of the fatigue test samples. The measurements were performed at an accelerating voltage of 120 kV and a current of 58 μA. The effective pixel size was 10 μm that enabled detecting of defects greater than 20 μm per spatial dimension. A total of 1583 projections were recorded with an exposure time of 500 ms and at a rotation step size 0.22°. The porosity measurement revealed that the samples had a density of 99.99% with porosity size ranging between 40 and 220 μm.

Fatigue test samples were extracted from the walls using a wire electric discharge machine in the vertical orientation where the loading axis was parallel to the build direction, Fig. 1b. Fatigue samples were designed according to ASTM E466 standard [27] with a gauge length and gauge diameter of 18 mm and 6 mm respectively, Fig. 1b. Prior to the fatigue testing, the gauge section of the samples was polished using 4000 grit SiC papers to reduce the average surface roughness as specified by ASTM E466. Fatigue testing was carried out on a 100 kN servo-hydraulic test machine under constant amplitude stress with a stress ratio of 0.1, at 50 Hz frequency.

After the sample failure, the fracture surface analysis was carried out using a Scanning Electron Microscope (SEM) with an operating voltage of 10 kV. For the EBSD measurements, samples were extracted on the *X-Z* plane. For this, the crack initiating defect was identified from the fracture surface analysis, Fig. 2a. One half of the corresponding fractured sample was used to extract the sample for EBSD analysis; schematic representation of the sample extraction plan is shown in Fig. 2b. The sample was cut perpendicular to the *X-Z* plane close to the crack initiation defect using a high precision cutting machine, Fig. 2c. The cut section was then periodically grounded, polished and observed

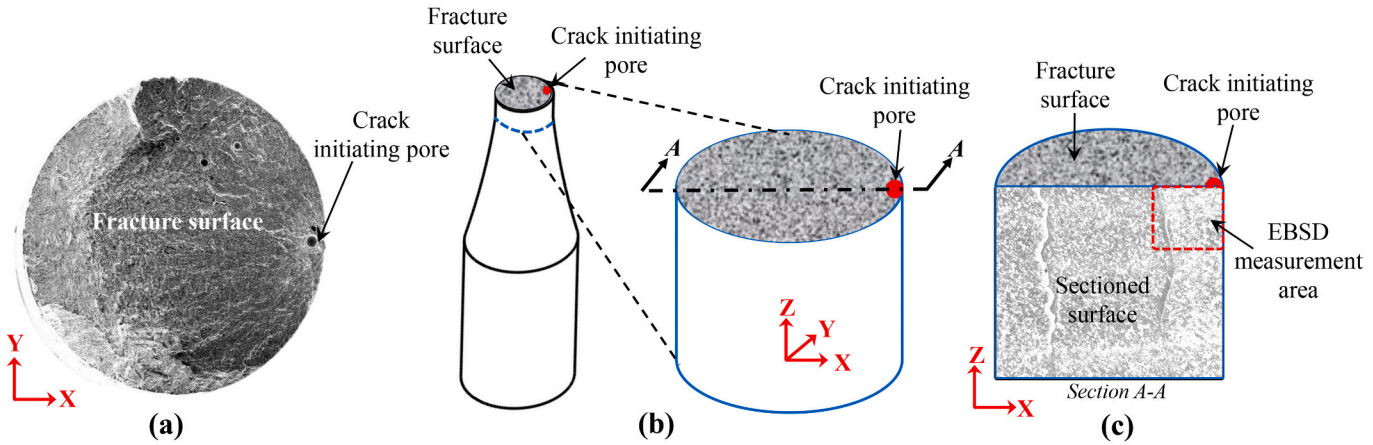

Fig. 2. (a) Example of a fracture surface showing the crack initiating defect, (b) schematic of a fractured sample showing sample extraction for EBSD analysis, (c) sample for EBSD analysis showing sectioned micrograph on the *X-Z* plane and location of EBSD measurement area around crack initiating defect.

Table 1
Slip directions and slip planes in Ti64, used for Schmid factor calculation.

Slip systems	Slip plane	Slip direction
Prismatic < a >	$\{10\bar{1}0\}$	$<\bar{1}2\bar{1}0>$
Basal < a >	{0002}	$<2\bar{1}\bar{1}0>$
1st order pyramidal < c + a >	$\{1\bar{1}01\}$	$<1\bar{2}\bar{1}\bar{3}>$

under an optical microscope until the crack initiation site was exposed for the EBSD analysis, Fig. 2c. Final polishing was carried out with 0.02 μm size colloidal silica. The area at and around the crack initiating defect was selected for EBSD measurements (highlighted in Fig. 2c). The EBSD measurements were carried out using a step size of 0.5 μm and at an operating voltage of 20 kV. Oxford Instruments Aztec HKL and Channel 5 imaging and post-processing software suites were employed for EBSD data analysis. The Schmid factor distribution was calculated along three different slip systems, i.e. the prismatic, basal and 1st order pyramidal. The slip planes and slip directions active in Ti hexagonal crystal lattice are presented in Table 1. For the EBSD measurements, the sample was tilted at 70° and the coordinate system was defined as $\phi = 0°$, $\varphi1 = -90°$ and $\varphi2 = 0°$ in the HKL software. To calculate the Schmid factor along the build direction, the loading direction (parallel to *Z*-axis in Fig. 2c) was defined as a 'rolling direction'. The output was obtained in the form of colour contour maps from where frequency distribution of each plane was extracted and is presented below. Based on the evidence from our previous [13,24] study, the presence of porosity defects did not cause non-uniform stress distribution. This is mainly due to the regular spherical shape of the porosity. Therefore, when considering the Schmid factor distribution within the stress field at the crack initiation area, we can broadly approximate the Schmid factor generated by HKL software as similar to the tensile load of smooth high cycle fatigue sample.

For optical microscopy (OM) microstructure analysis, separate samples were sectioned along the *X-Z* plane using identical preparation method to that of the EBSD samples. To reveal microstructure features by OM, polished samples were further etched with Kroll's reagent for 45 s.

3. Results and discussions

3.1. Microstructure analysis

A lower magnification optical micrograph of the overall microstructure along the *X-Z* plane is shown in Fig. 3a. The bulk microstructure consists of columnar prior β grains delineated by grain boundary α. The epitaxial growth of prior β grains is the direct consequence of large thermal gradient along the build direction (*Z*) perpendicular to the base plate. The deposited material will act as heat sink during the deposition, whereas the plasma heat source above will provide additional heat. Previous study on WAAM built Ti64 has showed that these columnar grains grew across the entire build height and had an average grain width of 1 to 2 mm [28]. Such a columnar microstructure is typically observed in other AM processes as well [29–31]. In Fig. 3a, a white heat affected zone (HAZ) bands were present and are indicated by arrows. These HAZ bands were observed on the entire height of the Ti64 wall except in the last few layers. They have similar characteristics as that of HAZ observed in welding [32]. According to [33], these bands are caused by re-heating of previously consolidated layer near to the β-transus temperature during the deposition of a subsequent layer. A comprehensive description and analysis of HAZ regions in AM can be found in [33]. Similar HAZ bands were reported in the wire feed [34], powder feed [33] and power bed [35] AM processes. However, the appearances of HAZ bands are more pronounced in the wire and powder feed AM process compared to powder bed process, due to higher heat input and deposition rates, along with greater layer height.

Within the columnar prior β grains, a transformed α + β microstructure with Widmanstätten and a colony morphology with considerable variation in the colony size were observed. Such heterogeneous microstructure was present in the entire deposited wall and was a consequence of complex thermal cycles experienced during the deposition dictated by the peak temperature, the time at the temperature, and the cooling rates experienced by each deposited layer [28]. In general, β → α transformation in Ti64 obeys Burgers orientation relationship [36]. During the transformation, α grew into the prior β grains with transformation microstructure very sensitive to the cooling rate. Because of the higher cooling rates, the nucleation rate was higher and allowed formation of larger number of grain boundary α (α_{GB}) nodules simultaneously, leading to a smaller colony size. Furthermore, the formation of large α colonies was prevented by increased driving force that enabled α nucleation at pre-existing α laths within the prior β grain. Thus, a small colony size consisted of smaller α lath width that can be observed in Fig. 3b [15]. On the other hand, at lower to moderate cooling rates only small number of α_{GB} nodules were formed within the prior β grain due to under-cooling below the β transus temperature. As a result the already formed colonies grew without interfering each other and formed large colonies of α, Fig. 3c and d [15]. However, higher cooling rates observed in selective laser melting AM process led to metastable α′ which is detrimental to the mechanical properties [1]. Formation of such metastable phases has not been reported in WAAM built Ti64 [28] and was not observed in this research

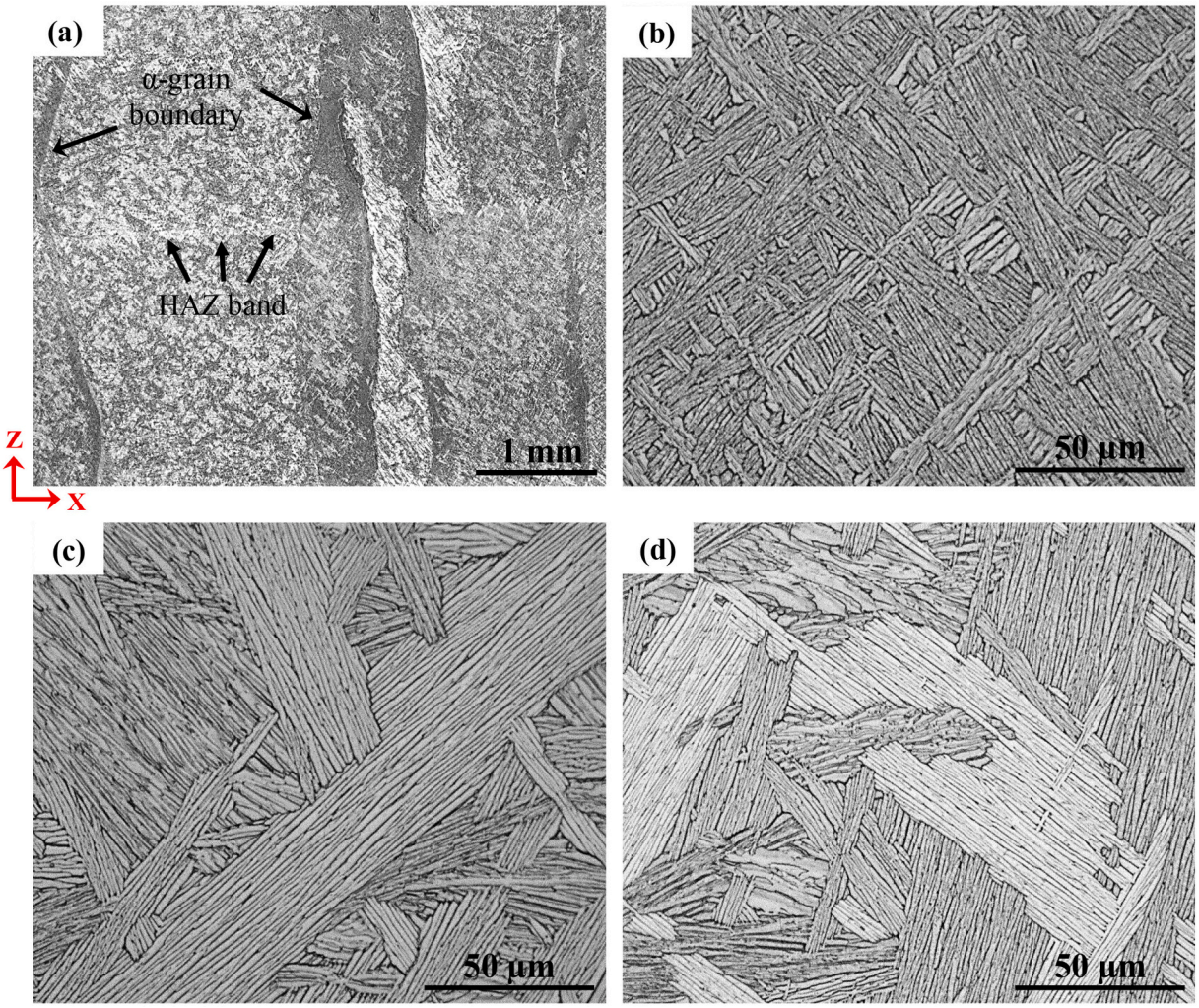

Fig. 3. Optical micrographs of WAAM Ti64 along the *X-Z* plane (for details please see Fig. 1); (a) low magnification macrostructure showing the columnar prior β-grains; the α grain boundary and HAZ band are indicated; higher magnification images within a deposited layer showing the microstructure variations of (b) the Widmanstätten morphology consisting of α (light colour) and β (dark colour) phases; (c) and (d) lamellar morphology showing different sizes of colonies.

either. This was mainly due to lower cooling rates associated with the WAAM process. Fig. 3d also indicated contrast between neighbouring α colonies. This is caused due to the variation in the reflectivity of light from the low contrast zones, which could be a result of different crystallographic orientation of trivalent α colonies affecting the etching behaviour. Zhao et al. [37] found similar regions in single bead WAAM Ti64 and concluded that this variation is caused by the differences in interaction of the etchant with the colonies.

3.2. Fatigue life and fractography

Fatigue test results from [22] are presented in Fig. 4a. A large scatter in samples tested at the same applied stress is apparent. In order to understand the fatigue life scatter, the geometrical characteristics of the internal defects, i.e., the size and location of crack initiating defects, were analysed through fracture surfaces analysis using SEM on all the selected samples at three stress levels. These selected samples are those with solid symbols in Fig. 4a. Fracture surface study confirmed that the crack always initiated from a defect, and the crack initiating defect size varied between 47 µm to 230 µm. However, a poor correlation was found between the fatigue life and the crack initiating defect size (Table 2). Crack initiation from defects along with heterogeneous microstructure in WAAM Ti64 might have influenced the crack initiation life, and thereby overall scatter in the fatigue life. Therefore, along with the crack initiation geometrical characteristics, a detailed study on crystallographic orientation of α and the average α lath width around the crack initiating defect was carried out for the selected samples in Fig. 4a.

In our previous study [13], we have demonstrated through finite element modelling that the location of defect influenced the stress concertation factor. When the ratio of defect distance from the free surface (x) to the defect diameter (d) was greater than 0.8, the interaction between the free surface and defect was negligible and had no influence on the stress concentration factor. Based on this study the defect sizes and their locations were categorised into two classes; (i) embedded defects - if the $x/d > 0.8$, and (ii) surface defects – if the $x/d < 0.8$, Fig. 4b. From the study of the fracture surfaces, it was found that the cracks were initiated from embedded defects in all samples selected for study at 700 MPa, whereas cracks initiated from surface defects in samples tested at 600 MPa and 500 MPa. To provide better presentation of the results, samples were labelled based on the size of the crack initiating defect (smallest to largest) at each stress level, i.e. at 700 MPa S1, S2, S3 and S4, at 600 MPa, S5 and S6 and at 500 MPa, S7, S8 and S9 respectively. The results are presented in Table 2, which shows the defect size, its distance from the free surface, and corresponding fatigue life of the sample.

3.3. Crack initiation from embedded defects

Fig. 5 shows fatigue life vs. crack initiating defect size for the selected samples. Irrespective of the crack initiating defect location (i.e.

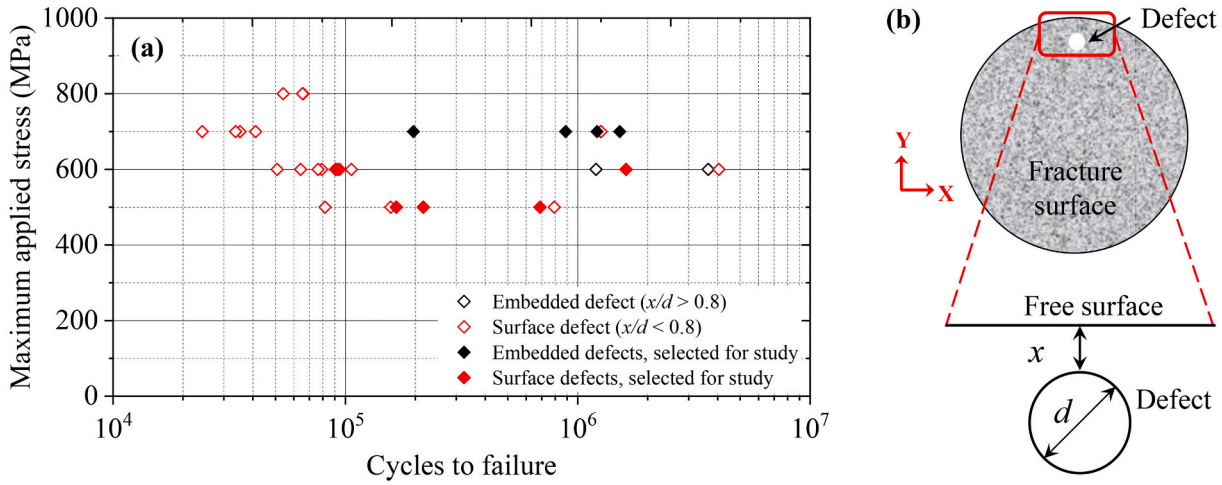

Fig. 4. (a) Fatigue test results indicating defect location where crack was initiated; redrawn from [22]; filled symbols represent samples selected for this study; (b) schematic of defect location and definition of distance to sample surface.

either crack initiation from embedded or surface defect), data presented in the Fig. 5 did not show any correlation between the defect size and the fatigue life. At 700 MPa applied stress, cracks were initiated from an embedded defect of 47 μm, 60 μm, 106 μm and 229 μm diameter in samples S1, S2, S3 and S4 respectively. In the case of S1 and S2, the crack initiated from a similar defect size. However, the fatigue life of S2 is approximately half of that in S1. Similarly, the crack initiating defect size of S4 is approximately four times and two times larger than S2 and S3, but the fatigue life of S4 was found to be approximately 1.5 times and six times longer than S2 and S3 respectively (refer Fig. 5). Moreover, the defect in S4 was closer to the free surface compared to S2 and S3. From this observation, it is evident that the defect size and its location were not the only factors causing fatigue life scatter. On the other hand, Murakami and Endo [14,38] suggested a fracture mechanics approach where they have considered the projected area of the crack initiating defect to represent an effective crack size for embedded defects. The proposed stress intensity factor range (ΔK) used the $\sqrt{area}$ of the defect instead of a simple crack length a as shown in Eq. (1) [14].

$$\Delta K = C \times \Delta\sigma\sqrt{\pi\sqrt{area}} \quad (1)$$

where ΔK is the stress intensity factor range, parameter C is 0.65 for surface defects or 0.5 for embedded defects, $\Delta\sigma$ is the applied stress range, and $\sqrt{area}$ is square root of the projected area of the defect. From Eq. (1), it can be noticed that ΔK is directly proportional to the defect size. To understand the effect of microstructure (α lath width and α colony size) and the crystallographic orientation at and around the crack initiating defects on the fatigue life scatter, EBSD measurements were performed on all samples.

Fracture surfaces for samples at 700 MPa are presented in Fig. 6 along with respective high magnification SEM images showing crack initiating defects. The crack initiating defects appeared to be spherical or near spherical in shape. EBSD orientation maps for samples at 700 MPa are presented in Fig. 7 and confirm considerable variations in the crystallographic orientation of α in S1, S2, S3 and S4 samples. Previous studies have demonstrated that the variation in

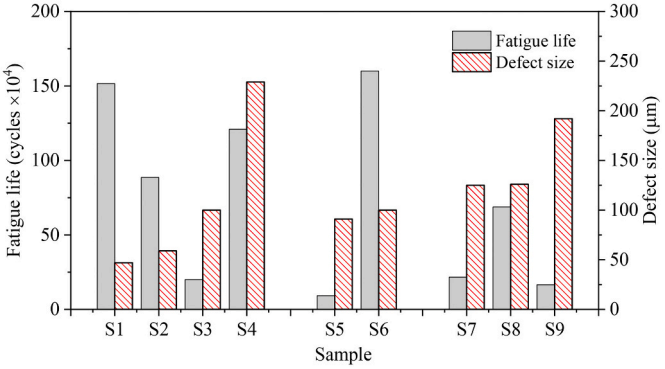

Fig. 5. Fatigue life and crack initiating defect size for samples under maximum applied stress 700 MPa (S1-S4), 600 MPa (S5, S6) and 500 MPa (S7-S9).

crystallographic orientation influences the slip activity and thereby the fatigue life [39–41]. The most common slip systems in Ti64 are basal < a >, prismatic < a > and pyramidal < c + a > [34,41]. When a polycrystalline material is plastically deformed under uniaxial loading, slip will initiate in grains that are favourably orientated and result in micro yielding. Further increase in the deformation would lead to a redistribution or transfer of the local stresses from softer grain families to the harder grain families which are not favourably oriented for slip [42].

To identify the active slip system as a function of grain orientation with respect to the loading direction and the *c*-axis of a given grain, distribution of the Schmid factor values for three active slip systems, i.e. < a > basal, < a > prismatic and < c + a > pyramidal, obtained from EBSD analysis were mapped and are presented in Fig. 7 for comparison. Schmid factor describes the slip plane and the slip direction in a material that can resolve the most shear stress, higher the Schmid factor, the more likely that the respective slip system will be activated [43]. In Fig. 7, Schmid factor distribution analysis shows that S2 had the highest basal slip Schmid factor, whereas S4 had higher

Table 2
Fatigue life of samples with the defect details that led to crack initiation.

Maximum applied stress (MPa)	700				600		500		
Sample label	S1	S2	S3	S4	S5	S6	S7	S8	S9
Fatigue life (×10⁴)	152	89	20	121	9	160	22	69	17
Defect diameter (μm)	47	59	106	229	91	100	125	126	192
Defect distance to the free surface (μm)	1900	600	670	500	Surface defect	Surface defect	Surface defect	Surface defect	Surface defect

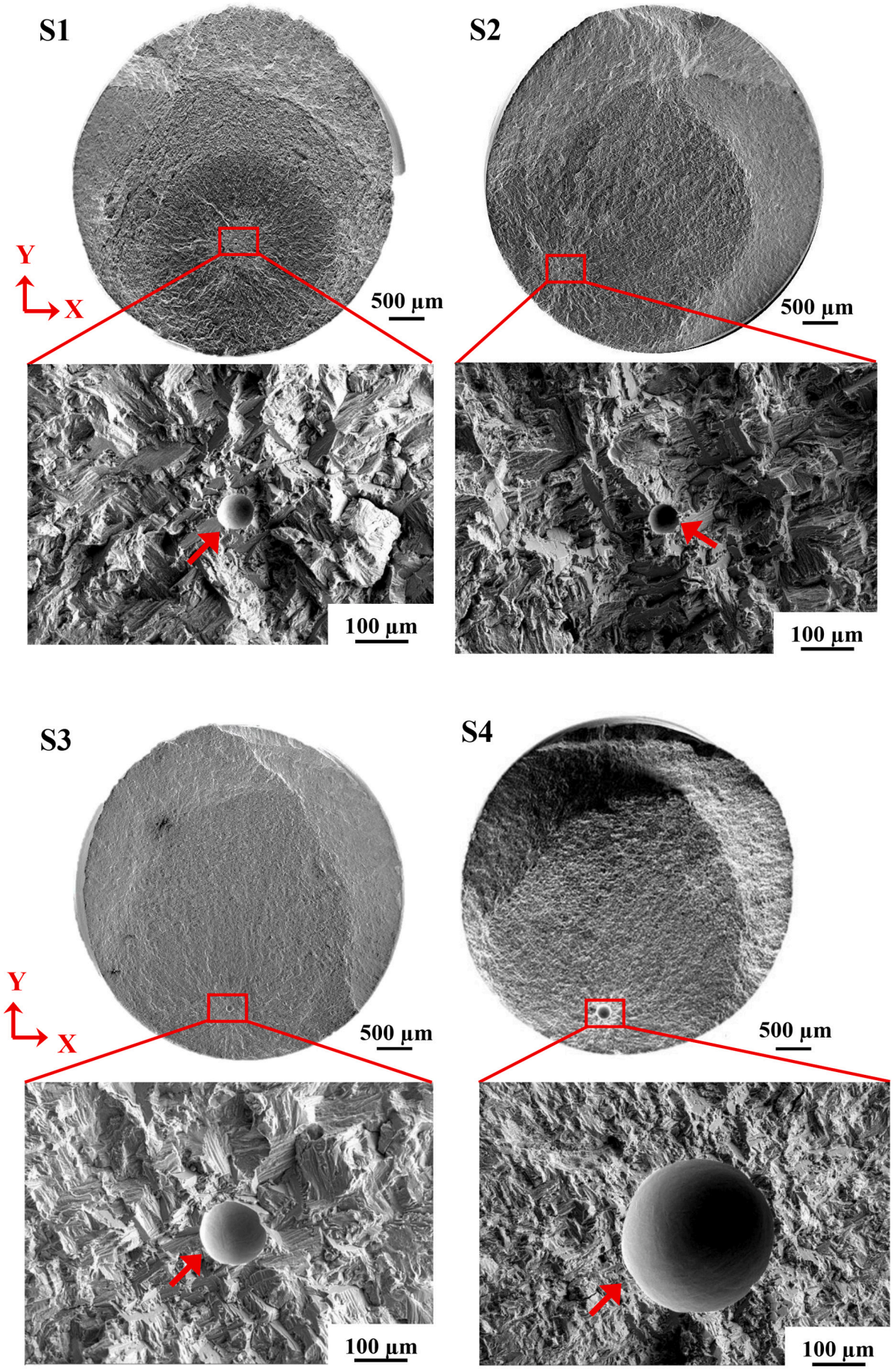

(caption on next page)

Fig. 6. SEM images of fracture surfaces showing the embedded defect for the 700 MPa sample group. The crack initiating defect is indicated with an arrow.

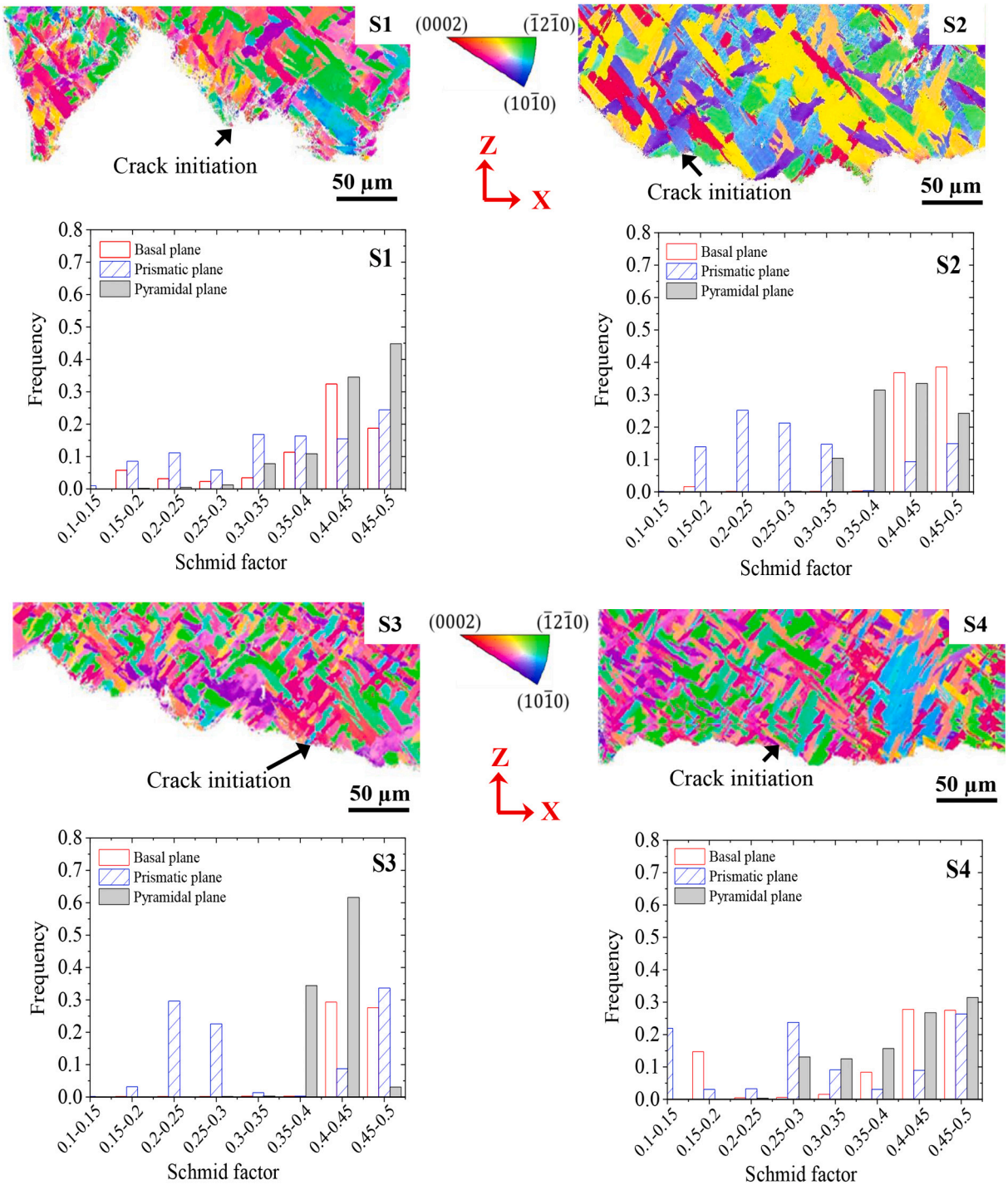

Fig. 7. EBSD orientation maps of 700 MPa fractured samples showing crack initiation location and Schmid factor distribution analysis. The build and loading directions are parallel to *Z*-axis.

pyramidal slip Schmid factor distribution at the 0.45–0.5 value range. Under the fatigue loading, activation of slip mainly depends on the critical resolved shear stress (CRSS) and the Schmid factor, where CRSS is the shear stress component, resolved in the direction of slip and required for initiating slip. According to [44], CRSS required to initiate slip in Ti64 for the prismatic < a > <$\bar{1}2\bar{1}0$>{$10\bar{1}0$}, basal < a > <$2\bar{1}\bar{1}0$ > {0002} and pyramidal < c + a > <$1\bar{2}\bar{1}\bar{3}$>{$1\bar{1}01$} slip systems is 370, 420 and 590 MPa, respectively. If the basal plane is parallel to the loading direction (perpendicular to *c*-axis of the grain), prismatic slip system <$\bar{1}2\bar{1}0$> {$10\bar{1}0$} is dominant, while pyramidal slip system <$1\bar{2}\bar{1}\bar{3}$> {$1\bar{1}01$} is dominant when the basal plane is perpendicular to the loading direction. On the other hand, basal slip system <$2\bar{1}\bar{1}0$> {0002} will become active if the misorientation angle between the loading direction and the basal plane < a > is between 10° to 66.7° [45]. Further increase in the misorientation angle from 66.7° to 90° will lead to the activation of the prismatic slip system [45].

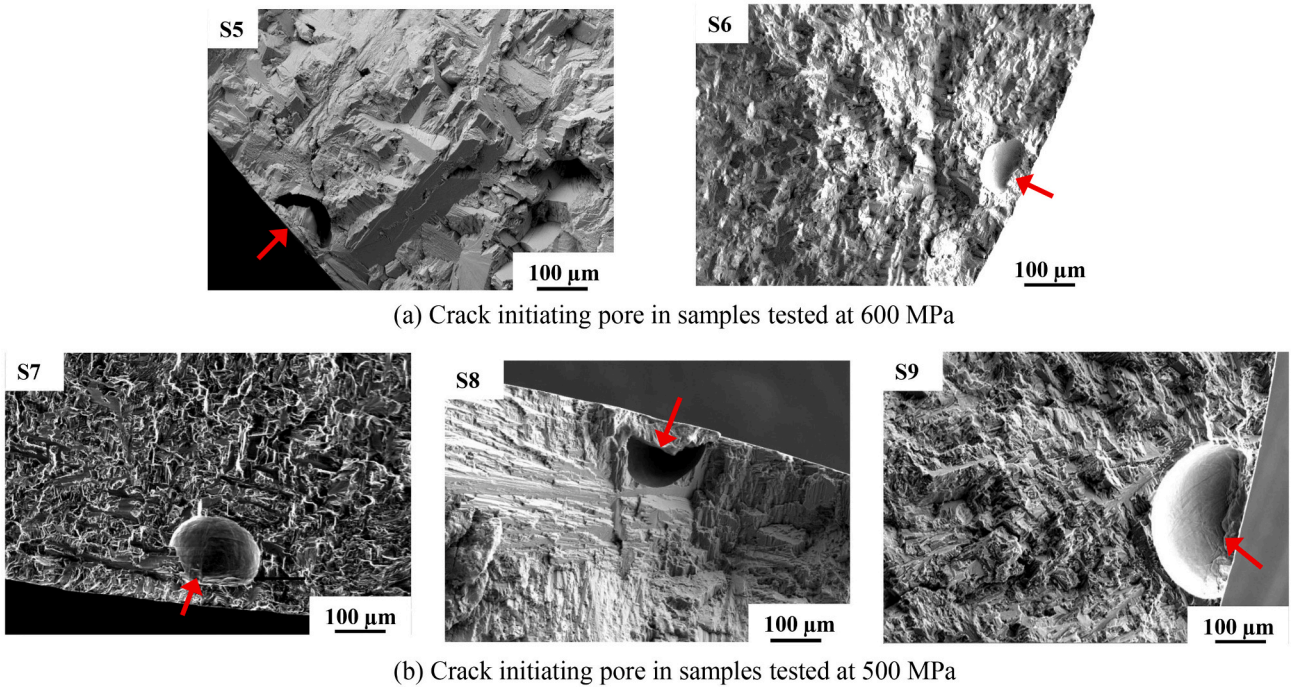

Fig. 8. SEM images of fracture surfaces showing the crack initiating defect (indicated with an arrow) for samples tested at 600 and 500 MPa.

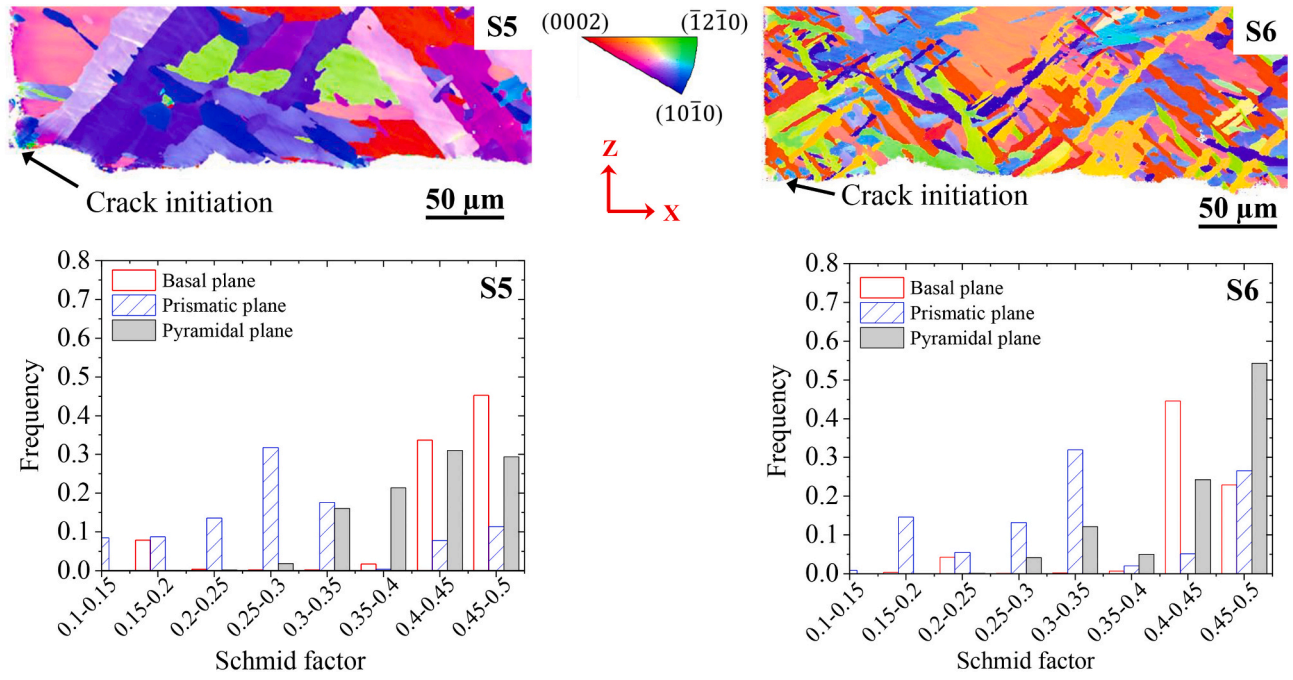

Fig. 9. EBSD orientation maps of 600 MPa fractured samples showing crack initiation location and Schmid factor distribution analysis in S5 and S6. The build and loading direction are parallel to *Z*-axis.

Based on the above, despite crack initiated from a smaller defect size, the lower CRSS associated with basal slip in S2 resulted in lower fatigue life than S4. However, when the fatigue results were compared between S2 and S1, a 20% decrease in the defect size in the case of S1 resulted in a 100% increase in the fatigue life compared to S2. Moreover, when S3 was compared with S4, it was observed that the smaller defect has resulted in approximately 80% decrease in the fatigue life. Schmid factor analysis showed negligible pyramidal slip Schmid factor distribution at 0.45–0.5 in the case of S3, which would have initiated the crack early owing to the lower CRSS associated with the prismatic slip, resulting in lower fatigue life compared to S4. The higher values of the CRSS associated with the pyramidal slip system might have delayed the onset deformation and the crack initiation under cyclic loading, therefore higher fatigue life was found in S1 and S4 compared to S2. While in the case of S3 the lower value of the CRSS of the prismatic slip system initiated an early crack resulting in a reduced fatigue life, despite the smaller defect than S4.

3.4. Crack initiation from surface defects

At 600 MPa, S5 and S6 showed crack initiation from similar size defect, but the fatigue life of S5 was only 6% of S6. Similarly, the crack was

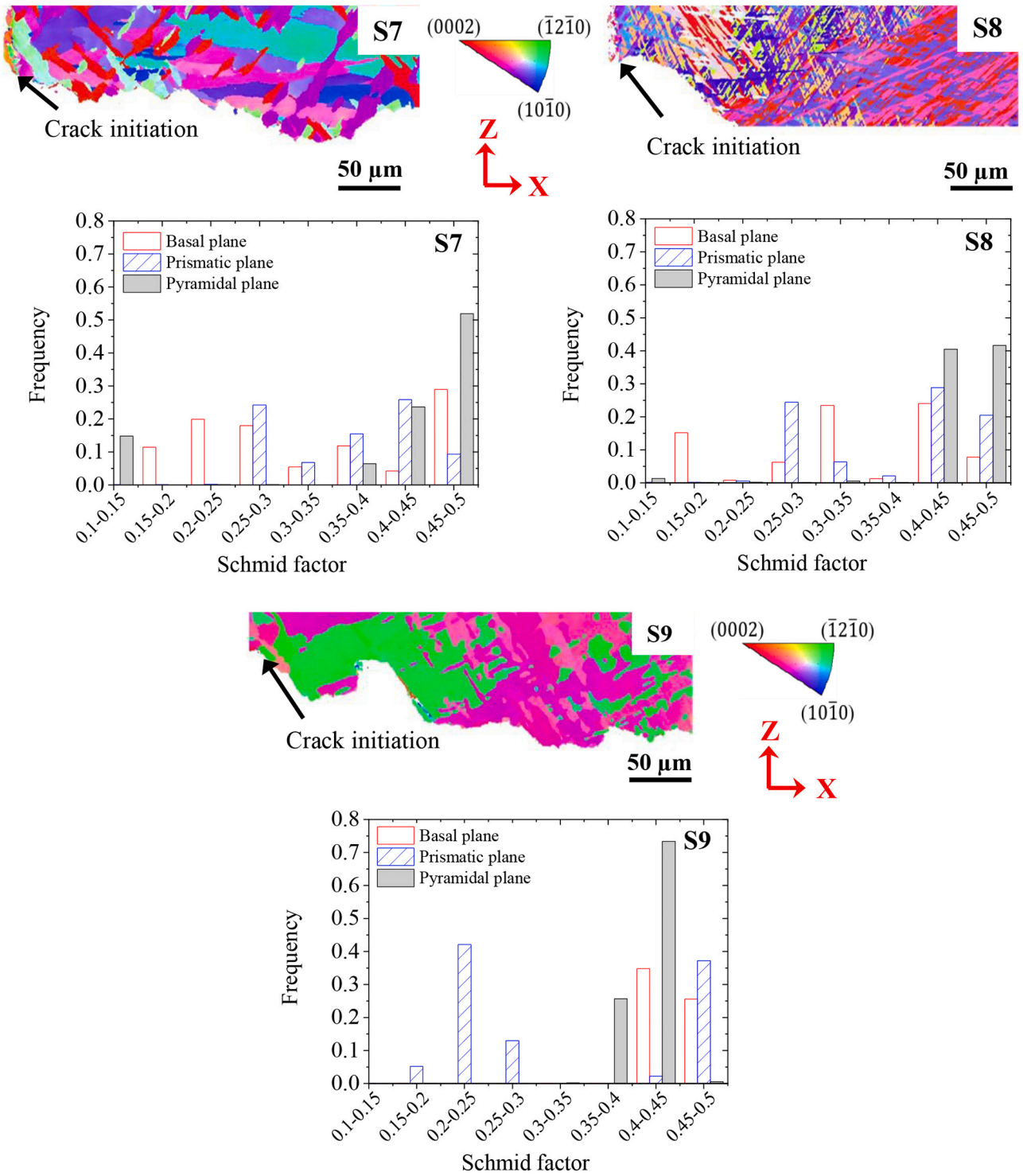

Fig. 10. EBSD orientation maps of 500 MPa fractured samples showing crack initiation location and Schmid factor distribution analysis in S7, S8 and S9. The build and loading direction are parallel to *Z*-axis.

initiated from a similar defect size in S7 and S8 tested at 500 MPa. However, the fatigue life of S8 was three times higher than S7. On the other hand, despite the crack initiating defect is 1.5 times larger in S9 compared to S7, they both showed similar fatigue life. This confirms that there is no correlation between the crack initiating defect size and fatigue life.

Fig. 8 shows SEM images of fracture surfaces of 600 and 500 MPa samples showing crack initiating defects which appeared to be spherical or near spherical in shape. EBSD measurements were carried out to investigate the role of crystallographic orientation and grain size distribution on the fatigue life scatter in 600 and 500 MPa samples.

EBSD analysis for S5 and S6 samples tested at 600 MPa are presented in Fig. 9 along with the distribution of the Schmid factor values calculated for each slip system. Sample S6 showed higher pyramidal slip Schmid factor distribution, whereas S5 had a higher basal slip Schmid factor distribution. The higher activity of the pyramidal slip system $< c + a > <1\bar{2}1\bar{3}>$ along with the high Schmid factor distribution of the basal and prismatic systems in S6 might have influenced the crack initiation and has resulted in the fracture along different slip

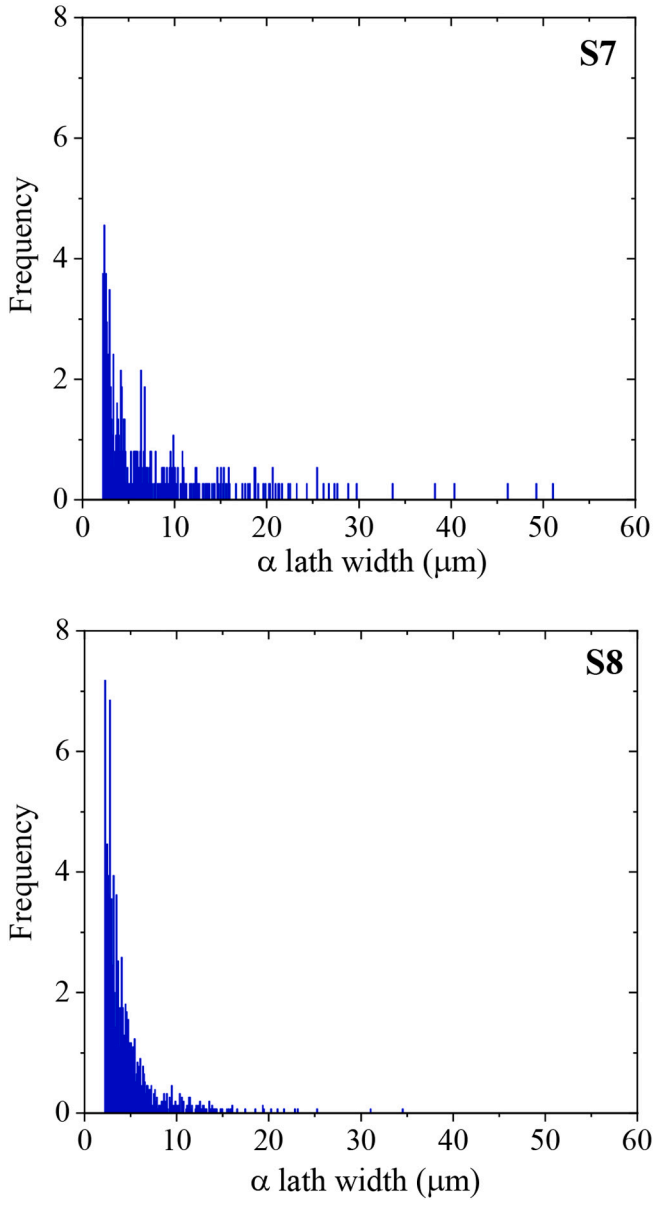

Fig. 11. Distribution of α lath size obtained from EBSD analysis for tests S7 and S8.

systems. In contrast, S5 has higher frequency of the basal < a > < 0002 > slip system and lower distribution of the pyramidal slip system < c + a > <$1\bar{2}1\bar{3}$> with values of the Schmid factor between 0.45 and 0.5. Therefore, the crack might have initiated along the basal slip in S5. Overall, the strong basal slip system active in S5 resulted in a lower fatigue life associated with lower value of CRSS required to initiate slip, whereas higher distribution of pyramidal slip systems in S6 resulted in the higher fatigue life than S5.

At 500 MPa, although S7 had higher pyramidal slip system distribution of Schmid factor values between 0.45 and 0.5 (Fig. 10), its fatigue life was only 30% of S8. This indicates that the Schmid factor alone could not explain the scatter in the fatigue life of S7 and S8. Therefore, further microstructure analysis was carried out. From the microstructure presented in Fig. 3 it is evident that there was a variation in the local microstructure within the macro zone of the samples. The multiple thermal cycles (melting-solidification) during WAAM processes directly resulted in complex microstructures that are varying spatially within the build. This was also confirmed by the EBSD micrographs presented in Fig. 10.

Crack initiation, as well as the whole fatigue process were controlled by cyclic plastic deformation. When the material was subjected to a large number of fatigue cycles, dislocation pile-ups occurred and accumulation of pileups resulted into persistent slip bands (extrusions and intrusions), which were formed due to slip along the favourable slip plane. These extrusions and intrusions acted as micronotches or stress concentration locations and promoted additional slip that led to fatigue crack nucleation [46]. In Ti64, HCF strength, i.e. the resistance to crack initiation, depends primarily on the resistance to dislocation motion. Consequently, the slip length distance and the α colony size or α lath width dictates HCF strength [15,45]. When considering the influence of α lath width, it has been demonstrated that the increased α lath width would cause decreased fatigue life due to increased slip length. Similarly, when considering the colony size, the increased colony size would lead to decrease of the fatigue life due to increased slip length [15]. Although both α phase and β matrix will deform independently, slip can be easily transferred across the incoherent α/β interface resulting in the crack to initiate from the α phase [15].

Therefore, a detailed analysis of the α lath width and of the α colony size at the crack initiation location may provide further insights into the fatigue life scatter in S7 and S8. Although α lath width variation was observed for all samples in Fig. 10a, a statistical distribution would provide further insights into the microstructure around the crack initiation site. The α lath width distribution was obtained from the ESBD analysis for S7 and S8 is presented in the Fig. 11. The graph of S7 presented in Fig. 11 is skewed towards the right, showing that S7 has a considerably higher distribution of larger α laths, whereas S8 showed a large distribution of smaller α laths (skewed towards the left). Although S8 showed a lower frequency of pyramidal distribution, the presence of smaller α laths required higher stress/fatigue cycles to activate slip and to initiate a fatigue crack. The large α laths distribution has resulted in lower fatigue life in S7, confirming that both crystallographic orientation of α and α lath width distribution at and around the defect contributes to the overall fatigue life, whereas larger defect size resulted in reduced fatigue life in S9.

4. Conclusions

In this study we investigated the role of the microstructure and the crystallographic orientation at and around the crack initiating defects, for both embedded and surface defects, by fracture surface analysis and the EBSD measurements. Based on the findings the following conclusions are drawn:

1. The primary factors behind the fatigue life scatter are due to the combined effect of the defect size, its location, and variations of the crystallographic orientation and microstructure at and around the crack initiation defect. The size of the defect alone cannot correlate with the fatigue life; hence the large scatter found in the S-N curves.
2. For the same defect size and at a similar location with the same applied stress, scatter in the fatigue life can be partially explained by the local variations on crystallographic orientation of α. The samples with the higher distribution of Schmid factors for pyramidal slip systems had longer fatigue life due to the higher critical resolved shear stress required for the cyclic slip to occur.
3. Considering the microstructure influence, a large number of smaller α laths at and around the crack initiating defects contributed to longer fatigue life, and vice versa.
4. If process induced porosity defects cannot be eliminated in additive manufactured titanium alloys, then the fatigue life could be improved by reducing the α lath width and creating a larger number of active pyramidal slip systems.

Declaration of competing interest

The authors declare that they have no known competing financial interests or personal relationships that could have appeared to influence the work reported in this paper.

Acknowledgements

The authors thank Cranfield University for providing experimental materials. Author MS also thanks the WAAMMat programme and Coventry University for the PhD studentship, and XZ acknowledges the Engineering and Physical Sciences Research Council (EPSRC) for supporting this research through the programme grant NEWAM (EP/R027218/1).

Data availability

The raw/processed data required to reproduce these findings cannot be shared at this time as the data also forms part of an ongoing study.

References

[1] S. Liu, Y.C. Shin, Additive manufacturing of Ti6Al4V alloy: a review, Mater. Des. 164 (2019) 107552, https://doi.org/10.1016/J.MATDES.2018.107552.
[2] A. Yadollahi, N. Shamsaei, Additive manufacturing of fatigue resistant materials: challenges and opportunities, Int. J. Fatigue 98 (2017) 14–31, https://doi.org/10.1016/j.ijfatigue.2017.01.001.
[3] P. Li, D.H. Warner, A. Fatemi, N. Phan, Critical assessment of the fatigue performance of additively manufactured Ti-6Al-4V and perspective for future research, Int. J. Fatigue 85 (2016) 130–143, https://doi.org/10.1016/j.ijfatigue.2015.12.003.
[4] J.J. Lewandowski, M. Seifi, Metal additive manufacturing: a review of mechanical properties, Annu. Rev. Mater. Res. 46 (2016) 151–186, https://doi.org/10.1146/annurev-matsci-070115-032024.
[5] A. Fatemi, R. Molaei, J. Simsiriwong, N. Sanaei, J. Pegues, B. Torries, N. Phan, N. Shamsaei, Fatigue behaviour of additive manufactured materials: an overview of some recent experimental studies on Ti - 6Al - 4V considering various processing and loading direction effects, Fatigue. Fract. Eng. M. (2019) 1–19, https://doi.org/10.1111/ffe.13000.
[6] S. Tammas-Williams, P.J. Withers, I. Todd, P.B. Prangnell, The influence of porosity on fatigue crack initiation in additively manufactured titanium components, Sci. Rep. 7 (2017) 7308, https://doi.org/10.1038/s41598-017-06504-5.
[7] G. Kasperovich, J. Hausmann, Improvement of fatigue resistance and ductility of TiAl6V4 processed by selective laser melting, J. Mater. Process. Technol. 220 (2015) 202–214, https://doi.org/10.1016/J.JMATPROTEC.2015.01.025.
[8] E. Wycisk, A. Solbach, S. Siddique, D. Herzog, F. Walther, Effects of defects in laser additive manufactured Ti-6Al-4V on fatigue properties, Phys. Procedia 56 (2014) 371–378, https://doi.org/10.1016/j.phpro.2014.08.120.
[9] S. Leuders, T. Lieneke, S. Lammers, T. Tröster, T. Niendorf, On the fatigue properties of metals manufactured by selective laser melting – the role of ductility, J. Mater. Res. 29 (2014) 1911–1919, https://doi.org/10.1557/jmr.2014.157.
[10] S. Leuders, M. Vollmer, F. Brenne, T. Tröster, T. Niendorf, Fatigue strength prediction for titanium alloy TiAl6V4 manufactured by selective laser melting, Metall. Mater. Trans. A 46 (2015) 3816–3823, https://doi.org/10.1007/s11661-015-2864-x.
[11] S. Beretta, S. Romano, A comparison of fatigue strength sensitivity to defects for materials manufactured by AM or traditional processes, Int. J. Fatigue 94 (2017) 178–191, https://doi.org/10.1016/j.ijfatigue.2016.06.020.
[12] J.C. Sobotka, M.P. Enright, R.C. McClung, Application of critical distances to fatigue at pores, Fatigue Fract. Eng. Mater. Struct. 42 (2019) 1646–1661, https://doi.org/10.1111/ffe.13004.
[13] R. Biswal, A.K. Syed, X. Zhang, Assessment of the effect of isolated porosity defects on the fatigue performance of additive manufactured titanium alloy, Addit. Manuf. 23 (2018) 433–442, https://doi.org/10.1016/j.addma.2018.08.024.
[14] Y. Murakami, Stress concentration, Met. Fatigue 3 (2019) 13–27, https://doi.org/10.1016/b978-0-12-813876-2.00002-9.
[15] G. Lutjering, Engineerig Materials and Processes, 2nd ed., Springer, Hamburg, 2007.
[16] W.G. Burgers, On the process of transition of the cubic-body-centered modification into the hexagonal-close-packed modification of zirconium, Physica 1 (1934) 561–586, https://doi.org/10.1016/S0031-8914(34)80244-3.
[17] F. Bridier, P. Villechaise, J. Mendez, Slip and fatigue crack formation processes in an α/β titanium alloy in relation to crystallographic texture on different scales, Acta Mater. 56 (2008) 3951–3962, https://doi.org/10.1016/j.actamat.2008.04.036.
[18] B. Oberwinkler, A. Lettner, W. Eichlseder, Multiscale fatigue crack observations on Ti-6Al-4V, Int. J. Fatigue 33 (2011) 710–718, https://doi.org/10.1016/j.ijfatigue.2010.11.024.
[19] H. Knobbe, P. Köster, H.J. Christ, C.P. Fritzen, M. Riedler, Initiation and propagation of short fatigue cracks in forged Ti6Al4V, Procedia Eng. 2 (2010) 931–940, https://doi.org/10.1016/j.proeng.2010.03.101.
[20] P. Åkerfeldt, M. Hörnqvist, R. Pederson, M. Antti, Electron backscatter diffraction characterization of fatigue crack growth in laser metal wire deposited Ti-6Al-4V, Mater. Charact. 135 (2018) 245–256, https://doi.org/10.1016/j.matchar.2017.11.041.
[21] F. Wang, S. Williams, P. Colegrove, A.A. Antonysamy, Microstructure and mechanical properties of wire and arc additive manufactured Ti-6Al-4V, Metall. Mater. Trans. A Phys. Metall. Mater. Sci. 44 (2013) 968–977, https://doi.org/10.1007/s11661-012-1444-6.
[22] R. Biswal, X. Zhang, A.K. Syed, M. Awd, J. Ding, F. Walther, S. Williams, Criticality of porosity defects on the fatigue performance of wire + arc additive manufactured titanium alloy, Int. J. Fatigue 122 (2019) 208–217, https://doi.org/10.1016/j.ijfatigue.2019.01.017.
[23] J. Gunther, D. Krewerth, T. Lippmann, S. Leuders, T. Troster, A. Weidner, H. Biermann, T. Niendorf, Fatigue life of additively manufactured Ti-6Al-4V in the very high cycle fatigue regime, Int. J. Fatigue 94 (2017) 236–245, https://doi.org/10.1016/j.ijfatigue.2016.05.018.
[24] R. Biswal, X. Zhang, M. Shamir, A. Al Mamun, M. Awd, F. Walther, A.K Syed, Interrupted fatigue testing with periodic tomography to monitor porosity defects in wire + arc additive manufactured Ti-6Al-4V, Addit. Manuf. (2019), https://doi.org/10.1016/j.addma.2019.04.026.
[25] C. de Formanoir, S. Michotte, O. Rigo, L. Germain, S. Godet, Electron beam melted Ti-6Al-4V: microstructure, texture and mechanical behavior of the as-built and heat-treated material, Mater. Sci. Eng. A 652 (2016) 105–119, https://doi.org/10.1016/j.msea.2015.11.052.
[26] H. Galarraga, D.A. Lados, R.R. Dehoff, M.M. Kirka, P. Nandwana, Effects of the microstructure and porosity on properties of Ti-6Al-4V ELI alloy fabricated by electron beam melting (EBM), Addit. Manuf. 10 (2016) 47–57, https://doi.org/10.1016/j.addma.2016.02.003.
[27] ASTM E466-15, Standard practice for conducting force controlled constant amplitude axial fatigue tests of metallic materials, ASTM International, West Conshohocken, Pennsylvania, 2015.
[28] F. Wang, S. Williams, P. Colegrove, A.A Antonysamy, Microstructure and mechanical properties of wire and arc additive manufactured Ti-6Al-4V, Metall. Mater. Trans. A. 44 (2012) 968.
[29] A.K Syed, B. Ahmad, H. Guo, T. Machry, D. Eatock, J. Meyer, M.E. Fitzpatrick, X. Zhang, An experimental study of residual stress and direction-dependence of fatigue crack growth behaviour in as-built and stress-relieved selective-laser-melted Ti6Al4V, Mater. Sci. Eng. A 755 (2019) 246–257, https://doi.org/10.1016/j.msea.2019.04.023.
[30] H. Sharma, D. Parfitt, A.K. Syed, D. Wimpenny, E. Muzangaza, G. Baxter, B. Chen, A critical evaluation of the microstructural gradient along the build direction in electron beam melted Ti-6Al-4V alloy, Mater. Sci. Eng. A 744 (2019) 182–194, https://doi.org/10.1016/j.msea.2018.12.016.
[31] Y. Zhai, H. Galarraga, D.A. Lados, Microstructure, static properties, and fatigue crack growth mechanisms in Ti-6Al-4V fabricated by additive manufacturing: LENS and EBM, Eng. Fail. Anal. 69 (2016) 3–14, https://doi.org/10.1016/j.engfailanal.2016.05.036.
[32] P. Kobryn, S. Semiatin, Microstructure and texture evolution during solidification processing of Ti–6Al–4V, J. Mater. Process. Technol. 135 (2003) 330–339, https://doi.org/10.1016/S0924-0136(02)00865-8.
[33] S.M. Kelly, S.L. Kampe, Microstructural evolution in laser-deposited multilayer Ti-6Al-4V builds: part II. Thermal modeling, Metall. Mater. Trans. A 35 (2004) 1869–1879, https://doi.org/10.1007/s11661-004-0095-7.
[34] B.A. Szost, S. Terzi, F. Martina, D. Boisselier, A. Prytuliak, T. Pirling, M. Hofmann, D.J. Jarvis, A comparative study of additive manufacturing techniques: residual stress and microstructural analysis of CLAD and WAAM printed Ti-6Al-4V components, Mater. Des. 89 (2016) 559–567, https://doi.org/10.1016/j.matdes.2015.09.115.
[35] S.S. Al-Bermani, M.L. Blackmore, W. Zhang, I. Todd, The origin of microstructural diversity, texture, and mechanical properties in electron beam melted Ti-6Al-4V, Metall. Mater. Trans. A 41 (2010) 3422–3434, https://doi.org/10.1007/s11661-010-0397-x.
[36] C. Leyens, M. Peters, Titanium and Titanium Alloys: Fundamentals and Applications, Wiley-VCH, 2003.
[37] H. Zhao, Microstructure heterogeneity in additive manufactured Ti-6Al-4V, PhD thesis University of Manchester, 2016.
[38] Y. Murakami, M. Endo, Effects of hardness and crack geometry on ΔK_{th} of small cracks, Mater. Sci. (1986) 275–293.
[39] A.L. Pilchak, R.E.A. Williams, J.C. Williams, Crystallography of fatigue crack initiation and growth in fully lamellar Ti-6Al-4V, Metall. Mater. Trans. A Phys. Metall. Mater. Sci. 41 (2010) 106–124, https://doi.org/10.1007/s11661-009-0064-2.
[40] V. Sinha, M.J. Mills, J.C. Williams, Crystallography of fracture facets in a near-alpha titanium alloy, Metall. Mater. Trans. A 37 (2006) 2015–2026, https://doi.org/10.1007/s11661-006-0144-5.
[41] I. Bantounas, T.C. Lindley, D. Rugg, D. Dye, Effect of microtexture on fatigue cracking in Ti–6Al–4V, Acta Mater. 55 (2007) 5655–5665, https://doi.org/10.1016/J.ACTAMAT.2007.06.034.
[42] J.L.W. Warwick, J. Coakley, S.L. Raghunathan, R.J. Talling, D. Dye, Effect of texture on load partitioning in Ti-6Al-4V, Acta Mater. 60 (2012) 4117–4127, https://doi.org/10.1016/J.ACTAMAT.2012.03.039.
[43] I. Bantounas, D. Dye, T.C. Lindley, The effect of grain orientation on fracture morphology during the high cycle fatigue of Ti-6Al-4V, Acta Mater. 57 (2009) 3951–3962, https://doi.org/10.1016/j.actamat.2009.04.018.
[44] F. Bridier, D.L. McDowell, P. Villechaise, J. Mendez, Crystal plasticity modeling of slip activity in Ti–6Al–4V under high cycle fatigue loading, Int. J. Plast. 25 (2009) 1066–1082, https://doi.org/10.1016/J.IJPLAS.2008.08.004.
[45] S. Hémery, P. Nizou, P. Villechaise, In situ SEM investigation of slip transfer in Ti-6Al-4V: effect of applied stress, Mater. Sci. Eng. A 709 (2018) 277–284, https://doi.org/10.1016/j.msea.2017.10.058.
[46] S. Suresh, Fatigue of materials, 2nd ed., Cambridge University Press, 1998.